

# Optical Studies on the Phase Transitions in $\text{YBaMn}_2\text{O}_6$ Single Crystals

Rea Divina Mero, Kirari Ogawa, Shigeki Yamada, and Hsiang-Lin Liu\*

Cite This: *ACS Omega* 2021, 6, 22137–22150

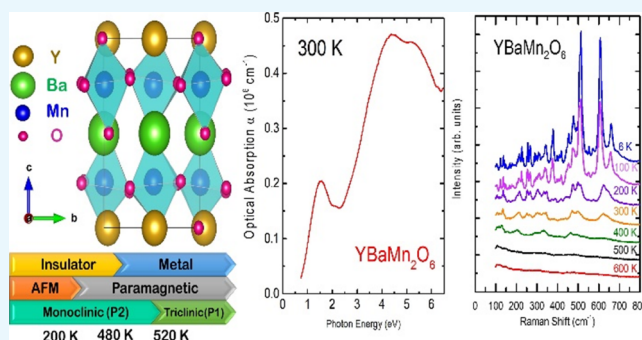
Read Online

ACCESS |

Metrics &amp; More

Article Recommendations

**ABSTRACT:** The double perovskite  $\text{YBaMn}_2\text{O}_6$  exhibited complex structural, magnetic, and charge/orbital ordering phase transitions. In this paper, we investigated the correlation between the temperature-dependent optical response and complex phase transitions of  $\text{YBaMn}_2\text{O}_6$  single crystals through spectroscopic ellipsometry and Raman scattering spectroscopy. The room temperature optical absorption spectrum of  $\text{YBaMn}_2\text{O}_6$  revealed three bands of approximately 1.50, 4.05, and 5.49 eV. The lowest optical absorption band was assigned to on-site d–d transitions in Mn ions, whereas the other two optical features were assigned to charge-transfer transitions between the 2p states of O and 3d states of Mn. The room temperature Raman scattering spectrum revealed 25 phonon modes. Notably, the  $\text{MnO}_6$  octahedral tilting and bending modes between 360 and 440  $\text{cm}^{-1}$  increased in intensity at temperatures <200 K. Furthermore, several new phonon peaks appeared at temperatures <200 K, which were associated with charge ordering. Additionally, the magnetic order-induced changes were observed in the breathing modes, with reduced intensity of the 620  $\text{cm}^{-1}$  and a substantial enhancement of the 644  $\text{cm}^{-1}$  phonon peaks. The Jahn–Teller mode at approximately 496  $\text{cm}^{-1}$  exhibited strong hardening at temperatures <200 K, which indicated a linear correlation with the square of the magnetic susceptibility and thus revealed the occurrence of spin–phonon coupling. Anomalies in the phonon frequency, line width, and intensity observed near the phase transition temperatures highlighted the importance of lattice–charge–spin interactions in  $\text{YBaMn}_2\text{O}_6$ .



## 1. INTRODUCTION

The A-site-ordered double perovskites with a general formula of  $\text{RBA}_2\text{Mn}_2\text{O}_6$  consist of alternately stacked layers of  $\text{RO}$ ,  $\text{MnO}_2$ , and  $\text{BaO}$  along the  $c$ -axis. This creates a  $\text{MnO}_2$  square sublattice sandwiched between two types of rock-salt layers ( $\text{RO}$  and  $\text{BaO}$ ) with substantially different sizes depending on the  $R$  atom. When the temperature changes, complex regions of the charge/orbital ordered phase, ferromagnetic/antiferromagnetic phase, and metal/insulator phase are formed. The reduced disorder introduced by the mismatch of the  $R$  and  $\text{Ba}$  atoms results in random electronic potential.<sup>1,2</sup> This is crucial for colossal magnetoresistance (CMR) and the phase competition between the ferromagnetic metallic phase and the charge/orbital ordered insulating phase. The CMR property is promising for next-generation memory devices.<sup>3–6</sup> Moreover, double perovskites can also be utilized in novel devices with combined functionalities of their magneto-electronic, optical, thermal, and thermoelectric properties.<sup>7–9</sup>

Early reports on  $\text{RBA}_2\text{Mn}_2\text{O}_6$  compounds indicated that as the ionic radius  $R$  increases, the ground-state property shifts from a charge/orbital ordered insulator (first and second group) to an A-type antiferromagnetic metal with a competing ferromagnetic metal phase (third group).<sup>10,11</sup> The first group, consisting of  $R = \text{Ho}, \text{Y}, \text{Dy},$  and  $\text{Tb}$ , has the smallest radius

and exhibits a structural phase transition at high temperatures and a CE-type antiferromagnetic insulating phase transition at low temperatures.<sup>10,12</sup> The second group, consisting of  $R = \text{Eu}, \text{Sm},$  and  $\text{Gd}$ , exhibits similar phase transitions with the first group except for the structural transition at high temperatures.<sup>2,10</sup> Notably, the charge/orbital ordering temperature of the first and second groups decreases as the ionic radius  $R$  is increased. However, the Néel temperature ( $T_N$ ) does not significantly change upon  $R$  substitution.<sup>2,10–12</sup>

We recently reported the optical and vibrational properties of the double perovskite  $\text{NdBaMn}_2\text{O}_6$ ,<sup>13</sup> which belongs to the third group.  $\text{NdBaMn}_2\text{O}_6$  exhibits no tilting of the  $\text{MnO}_6$  octahedra due to  $\text{Nd}$  ions' relatively large size.  $\text{YBaMn}_2\text{O}_6$ , unlike  $\text{NdBaMn}_2\text{O}_6$ , has heavily tilted and distorted  $\text{MnO}_6$  octahedra. This is due to the large mismatch between the ionic radii of  $\text{Y}$  and  $\text{Ba}$  atoms. Previous results of the X-ray powder

Received: May 26, 2021

Accepted: August 13, 2021

Published: August 23, 2021



diffraction of the polycrystalline samples by Nakajima *et al.*<sup>14</sup> revealed that  $\text{YBaMn}_2\text{O}_6$  crystallizes at room temperature in a monoclinic structure. The lattice parameters are as follows:  $a = 3.901(9)$  Å,  $b = 3.898(1)$  Å,  $c = 7.602(2)$  Å,  $\beta = 90.2(1)^\circ$ , and  $V = 115.5(9)$  Å<sup>3</sup>.<sup>14</sup> This is described as a pseudotetragonal structure because  $a \approx b$  and  $\beta \approx 90^\circ$ .<sup>14</sup> A structural transition is observed at a high temperature of approximately 520 K. The crystal still assumes a monoclinic form, but it has a pseudo-orthorhombic structure wherein  $a > b$  and  $\beta \approx 90^\circ$ . The structural parameters at high temperatures are given as follows:  $a = 3.930(6)$  Å,  $b = 3.846(3)$  Å,  $c = 7.731(2)$  Å,  $\beta = 90.2(8)^\circ$ , and  $V = 116.9(8)$  Å<sup>3</sup>.<sup>14</sup> The results from the Rietveld refinement of the neutron diffraction by Nakajima *et al.*<sup>15</sup> indicated the space group structures. At 350 K, the structure can reliably be classified into the monoclinic  $P2$  space group. At temperatures higher than the structural transition temperature (520 K), the crystal assumes a triclinic  $P1$  symmetry. Williams *et al.*<sup>16,17</sup> also conducted a Rietveld refinement on the neutron diffraction data of the polycrystalline  $\text{YBaMn}_2\text{O}_6$  samples. Their structure and phase transition assignments differed from those of Nakajima *et al.*<sup>15</sup> They assigned the ground-state structure at 300 K to a triclinic  $P1$ , which persisted up to 473 K. At 498 K, the structure was no longer triclinic, as evidenced by the absence of (220) peak splitting and the presence of the (202) peak split, which characterizes a monoclinic structure. The space group was fitted to a monoclinic  $C2/m$ . Between 673 and 723 K, another structural transition occurred, and an orthorhombic  $Cmmm$  symmetry was observed.

Temperature-dependent magnetic susceptibility and resistivity measurements of the polycrystalline  $\text{YBaMn}_2\text{O}_6$  samples by Nakajima *et al.*<sup>14,15</sup> clearly revealed three successive transitions at 520, 480, and 200 K. At temperatures higher than 520 K,  $\text{YBaMn}_2\text{O}_6$  was paramagnetic with the metallic property. It transitioned from a paramagnetic metal into a paramagnetic insulator at 480 K. The electron spin resonance study in the paramagnetic region also exhibited discrepancies at 520 and 480 K.<sup>18</sup> Finally, at 200 K, it transitioned into an antiferromagnetic insulator.<sup>14,15</sup> This transition is usually accompanied by charge rearrangement in most  $\text{RBaMn}_2\text{O}_6$  compounds.<sup>2,10</sup> Moreover, Williams *et al.*<sup>16,17</sup> suggested that charge ordering occurs at 498 K. The divergence in the magnetic susceptibility between zero-field-cooled and field-cooled at 45 K as observed by Gao *et al.*<sup>19</sup> was attributed to spin glass behavior. The phase transitions and the crystal structure at room temperature are depicted in Figure 1.

To date, no optical and vibrational properties have been reported for  $\text{YBaMn}_2\text{O}_6$  single crystals. To fill this gap, we performed spectroscopic ellipsometry and Raman scattering measurements. Comparing the results of  $\text{YBaMn}_2\text{O}_6$  with those of other  $\text{RBaMn}_2\text{O}_6$  double perovskites, particularly  $\text{NdBaMn}_2\text{O}_6$ , can clarify the effects of  $\text{MnO}_6$  octahedral tilting and A-site cation substitution. Furthermore, the result can help establish agreement on the layout of the complex physics of these materials and elucidate the effects of strong correlations between lattice, charge, and spin degrees of freedom in  $\text{YBaMn}_2\text{O}_6$ .

## 2. RESULTS AND DISCUSSION

**2.1. Electronic Excitations.** Figure 2 indicates the room temperature absorption spectrum of  $\text{YBaMn}_2\text{O}_6$  obtained through spectroscopic ellipsometry analysis.<sup>13</sup> We observed peaks centered at 1.50, 4.05, and 5.49 eV, which were fitted

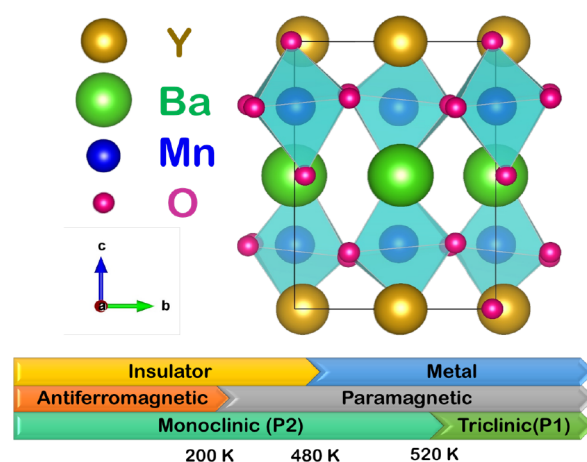


**Figure 1.** Crystal structure of  $\text{YBaMn}_2\text{O}_6$  at room temperature and a schematic depicting the electric, structural, and magnetic properties of  $\text{YBaMn}_2\text{O}_6$ .

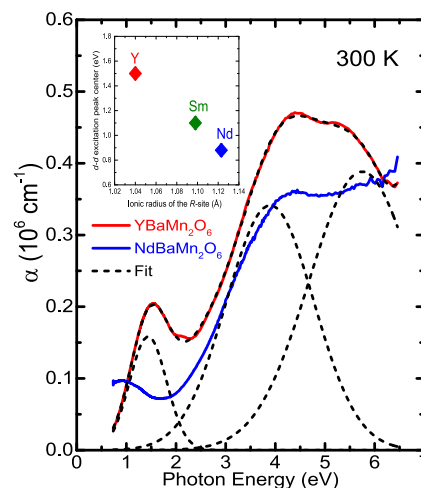


**Figure 2.** Room temperature optical absorption spectra of  $\text{YBaMn}_2\text{O}_6$  and  $\text{NdBaMn}_2\text{O}_6$ . The dashed lines denote the optimal fit of  $\text{YBaMn}_2\text{O}_6$  using the Lorentzian model. The inset illustrates the  $R$ -site atomic radii dependence of on-site  $d$ - $d$  transitions in Mn ions. The plot for  $\text{NdBaMn}_2\text{O}_6$  is adapted from ref 13. No subject to Copyright.

with Lorentz oscillators.<sup>20</sup> The high energy peaks at 4.05 and 5.49 eV originated from the charge-transfer transitions from O 2p to Mn 3d orbitals. The origin of these high energy peaks is clearly established in the literature.<sup>4,21,22</sup> The peak at 1.50 eV can be attributed to Mn  $d$ - $d$  transitions.<sup>22</sup> The absorption spectrum of  $\text{NdBaMn}_2\text{O}_6$  is also illustrated in Figure 2. We noticed that the peak intensity of  $\text{YBaMn}_2\text{O}_6$  was relatively higher than that of  $\text{NdBaMn}_2\text{O}_6$ . The  $d$ - $d$  excitation peak was also more pronounced in  $\text{YBaMn}_2\text{O}_6$  but suppressed in  $\text{NdBaMn}_2\text{O}_6$ . This enhanced  $d$ - $d$  excitation peak explains the insulating behavior of  $\text{YBaMn}_2\text{O}_6$ , whereas the suppressed peak in  $\text{NdBaMn}_2\text{O}_6$  contributes to its metallic ground state. In the  $\text{RMnO}_3$  compounds,<sup>23</sup> a similar decrease was noted in the spectral weight in the low-energy absorption region ( $<3$  eV) as the  $R$  ion radii increased. This phenomenon correlated with the systematic increase of the Néel temperature ( $T_N$ ) as  $R$  ion radii increased. Coincidentally, the same behavior was exhibited by  $\text{RBaMn}_2\text{O}_6$  when the  $T_N$  of  $\text{NdBaMn}_2\text{O}_6$  (235 K) was higher than that of  $\text{YBaMn}_2\text{O}_6$  (200 K). Furthermore, the increase in spectral weight also correlated with an increase in

the charge and orbital ordering temperature of  $\text{RBaMn}_2\text{O}_6$ . These phenomena imply that the tilting disorder induced by the smaller  $R$  radii favors the charge/orbital ordering as well as the spin ordering due to the enhanced Jahn–Teller distortions. Next, as we examined the d–d peak center position of  $\text{RBaMn}_2\text{O}_6$  with  $R = \text{Y}, \text{Sm},$  and  $\text{Nd}$ , we observed a notable  $R$  site ion dependence. The d–d peak energy is summarized in the inset of Figure 2. The  $\text{SmBaMn}_2\text{O}_6$  d–d peak was reported by Akahoshi *et al.*<sup>2</sup> in their optical conductivity data, and it had a photon energy of approximately 1.1 eV. As the size of the  $R$  cation increased from Y to Nd, the d–d excitation peaks were shifted to lower energies. This shift was also related to the modification of Jahn–Teller distortions.<sup>4,21,24</sup>

**2.2. Vibrational Properties.** Figure 3 illustrates the room temperature polarized Raman scattering spectra of  $\text{YBaMn}_2\text{O}_6$ .

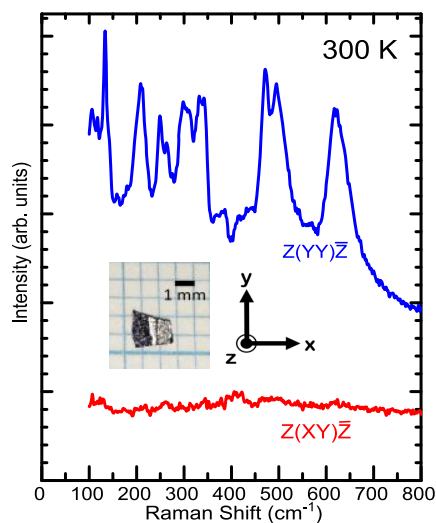


**Figure 3.** Room temperature polarized Raman scattering spectra and the optical image of  $\text{YBaMn}_2\text{O}_6$ . The notations used for the crystallographic directions are also given.

We performed the factor group analysis<sup>25</sup> on the crystal structures of polycrystalline  $\text{YBaMn}_2\text{O}_6$ , as proposed in the literature.<sup>14–17</sup> The details of the factor group analysis are provided in Tables 1–4. Nakajima *et al.*<sup>14,15</sup> proposed a monoclinic structure with the  $P2$  space group at room temperature. This structure contains 20 atoms in the unit cell with  $Z = 2$  and allows for 60 degrees of freedom. The  $P2$  structure tabulated in Table 1 results in  $25A + 32B$  vibrational modes, which are both Raman and infrared active. Only the

**Table 1. Factor Group Analysis of  $\text{YBaMn}_2\text{O}_6$  for Nakajima *et al.*'s<sup>14,15</sup> Monoclinic Structure with  $P2$  Space Group Assignment**

monoclinic $P2$ $\text{YBaMn}_2\text{O}_6$			
atom	Wyckoff notation	site symmetry	irreducible representation
Y	1c, 1a	$C_2$	$\Gamma_Y = 2A + 4B$
Ba	1b, 1d	$C_2$	$\Gamma_{Ba} = 2A + 4B$
Mn	3e (2)	$C_2$	$\Gamma_{Mn} = 6A + 6B$
O	1a, 1c	$C_2$	$\Gamma_O = 2A + 4B$
O	1b, 1d	$C_2$	$\Gamma_O = 2A + 4B$
O	2e (4)	$C_2$	$\Gamma_O = 12A + 12B$

$\Gamma_{\text{crystal}} = 26A + 34B$ ;  $\Gamma_{\text{acoustic}} = A + 2B$ ;  $\Gamma_{\text{vib}} = 25A + 32B$ . A and B are Raman and infrared active.

**Table 2. Factor Group Analysis of  $\text{YBaMn}_2\text{O}_6$  for Nakajima *et al.*'s<sup>14,15</sup> Triclinic Structure with  $P1$  Space Group Assignment**

triclinic $P1$ $\text{YBaMn}_2\text{O}_6$			
atom	Wyckoff notation	site symmetry	irreducible representation
Y (1)	1a	$C_1$ (1)	$\Gamma_Y = 3A$
Y (2)	1a	$C_1$ (1)	$\Gamma_Y = 3A$
Ba (1)	1a	$C_1$ (1)	$\Gamma_Y = 3A$
Ba (2)	1a	$C_1$ (1)	$\Gamma_Y = 3A$
Mn (1)	1a	$C_1$ (1)	$\Gamma_Y = 3A$
Mn (2)	1a	$C_1$ (1)	$\Gamma_Y = 3A$
Mn (3)	1a	$C_1$ (1)	$\Gamma_Y = 3A$
Mn (4)	1a	$C_1$ (1)	$\Gamma_Y = 3A$
O (1)	1a	$C_1$ (1)	$\Gamma_Y = 3A$
O (2)	1a	$C_1$ (1)	$\Gamma_Y = 3A$
O (3)	1a	$C_1$ (1)	$\Gamma_Y = 3A$
O (4)	1a	$C_1$ (1)	$\Gamma_Y = 3A$
O (5)	1a	$C_1$ (1)	$\Gamma_Y = 3A$
O (6)	1a	$C_1$ (1)	$\Gamma_Y = 3A$
O (7)	1a	$C_1$ (1)	$\Gamma_Y = 3A$
O (8)	1a	$C_1$ (1)	$\Gamma_Y = 3A$
O (9)	1a	$C_1$ (1)	$\Gamma_Y = 3A$
O (10)	1a	$C_1$ (1)	$\Gamma_Y = 3A$
O (11)	1a	$C_1$ (1)	$\Gamma_Y = 3A$
O (12)	1a	$C_1$ (1)	$\Gamma_Y = 3A$

$\Gamma_{\text{crystal}} = 60A$ ;  $\Gamma_{\text{acoustic}} = 3A$ ;  $\Gamma_{\text{vib}} = 57A$ . A is Raman and infrared active.

**Table 3. Factor Group Analysis of  $\text{YBaMn}_2\text{O}_6$  for Williams *et al.*'s<sup>16,17</sup> Triclinic Structure with  $P\bar{1}$  Space Group Assignment**

triclinic $P\bar{1}$ $\text{YBaMn}_2\text{O}_6$			
atom	Wyckoff notation	site symmetry	irreducible representation
Y	2i	$C_2$	$\Gamma_Y = 3A_g + 3A_u$
Ba	2i	$C_2$	$\Gamma_{Ba} = 3A_g + 3A_u$
Mn	2i (2)	$C_2$	$\Gamma_{Mn} = 6A_g + 6A_u$
O	2i (6)	$C_2$	$\Gamma_O = 18A_g + 18A_u$

$\Gamma_{\text{crystal}} = 30A_g + 30A_u$ ;  $\Gamma_{\text{acoustic}} = 3A_u$ ;  $\Gamma_{\text{vib}} = 30A_g + 27A_u$ .  $A_g$  is Raman active and  $A_u$  is infrared active.

**Table 4. Factor Group Analysis of  $\text{YBaMn}_2\text{O}_6$  for Williams *et al.*'s<sup>16,17</sup> Monoclinic Structure with  $C2/m$  Space Group Assignment**

monoclinic $C2/m$ $\text{YBaMn}_2\text{O}_6$			
atom	Wyckoff notation	site symmetry	irreducible representation
Y	4i	$C_2$	$\Gamma_Y = 2A_g + A_u + B_g + 2B_u$
Ba	4i	$C_2$	$\Gamma_{Ba} = 2A_g + A_u + B_g + 2B_u$
Mn	8j	$C_2$	$\Gamma_{Mn} = 3A_g + 3A_u + 3B_g + 3B_u$
O (1)	4h	$C_2$	$\Gamma_O = A_g + A_u + 2B_g + 2B_u$
O (2)	4g	$C_2$	$\Gamma_O = A_g + A_u + 2B_g + 2B_u$
O (3)	4i	$C_2$	$\Gamma_O = 2A_g + A_u + B_g + 2B_u$
O (4)	4i	$C_2$	$\Gamma_O = 2A_g + A_u + B_g + 2B_u$
O (5)	8j	$C_2$	$\Gamma_O = 3A_g + 3A_u + 3B_g + 3B_u$

$\Gamma_{\text{crystal}} = 16A_g + 12A_u + 14B_g + 18B_u$ ;  $\Gamma_{\text{acoustic}} = A_u + 2B_u$ ;  $\Gamma_{\text{vib}} = 16A_g(\text{R}) + 11A_u(\text{IR}) + 14B_g(\text{R}) + 16B_u(\text{IR})$ .  $A_g$  and  $B_g$  are Raman active and  $A_u$  and  $B_u$  are infrared active.

25A modes were expected in our selected configuration. Williams *et al.*<sup>16,17</sup> resolved the structure into a triclinic  $P\bar{1}$  shown in Table 3 that yields  $30A_g + 27A_u$  vibrational modes,

with the  $A_g$  mode being Raman active and  $A_u$  mode being infrared active. We identified 25 Raman active phonon modes at room temperature (see Table 5) and fitted them with

**Table 5. Raman Phonon Modes of  $YBaMn_2O_6$  at 210 and 300 K**

phonon mode	frequency ( $cm^{-1}$ )		symmetry
	210 K	300 K	
$\omega_2$	105	107	A
$\omega_3$	122	121	A
$\omega_4$	136	135	A
$\omega_5$	146	145	A
$\omega_7$	163	160	A
$\omega_9$	185	180	A
$\omega_{11}$	202	201	A
$\omega_{12}$	215	214	A
$\omega_{15}$	253	250	A
$\omega_{16}$	267	266	A
$\omega_{19}$	302	298	A
$\omega_{20}$	315	313	A
$\omega_{21}$	334	334	A
$\omega_{22}$	346	345	A
$\omega_{23}$	373	376	A
$\omega_{24}$	388	387	A
$\omega_{26}$	417	418	A
$\omega_{27}$	442	436	A
$\omega_{28}$	475	472	A
$\omega_{30}$	497	496	A
$\omega_{31}$	513	512	A
$\omega_{32}$	547	544	A
$\omega_{33}$	574	572	A
$\omega_{34}$	623	620	A
$\omega_{35}$	646	642	A

Lorentz oscillators.<sup>20</sup> This satisfies the monoclinic structure with the  $P2$  space group assigned by Nakajima *et al.*<sup>14,15</sup> Figure 3 displays the presence of all phonon peaks in the  $Z(Y\bar{Y})\bar{Z}$  scattering configuration, while they are suppressed in the  $Z(XY)\bar{Z}$  scattering configuration. We deduced from the polarization data that the phonon modes were of A symmetric character.

The temperature-dependent unpolarized Raman scattering spectra are illustrated in Figure 4. The temperature-dependent Raman scattering spectra generally exhibited a softening of the phonon frequencies as the temperature increased, which was accompanied by a broadening of the line width and a decrease in intensity. We stopped monitoring a phonon peak when its intensity dipped to <50 units following the subtraction of a constant background. Based on this condition, only 16 phonon modes tabulated in Table 6 remained at high temperatures (480 K).

At high temperatures (>498 K), a monoclinic structure with the  $C2/m$  space group was indexed by William *et al.*<sup>16,17</sup> This yields the vibrational modes of  $16A_g + 11A_u + 14B_g + 16B_u$ . The  $A_g$  and  $B_g$  modes are Raman active, while the  $A_u$  and  $B_u$  modes are infrared active (see Table 4). Meanwhile, at temperatures >520 K, a triclinic structure with the  $P1$  space group was assigned by Nakajima *et al.*<sup>14,15</sup> The factor group analysis of the  $P1$  structure detailed in Table 2 results in 57A modes, which are both Raman and infrared active. Table 6 summarizes the phonon modes identified at 540 K, which are noticeably less than the phonon modes expected in this

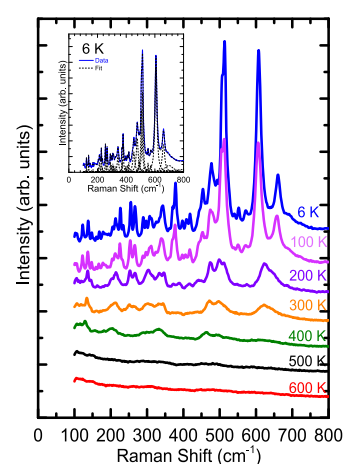


**Figure 4.** Temperature dependence of the unpolarized Raman scattering spectra of  $YBaMn_2O_6$ . The inset illustrates the results of fitting the spectrum obtained at 6 K by using the Lorentzian model.

**Table 6. Raman Phonon Modes of  $YBaMn_2O_6$  Identified at 480 and 540 K**

phonon mode	frequency ( $cm^{-1}$ )		symmetry
	480 K	540 K	
$\omega_2$	105	105	A
$\omega_3$	115	115	A
$\omega_4$	124		A
$\omega_5$	140		A
$\omega_7$	149	146	A
$\omega_{12}$	201	202	A
$\omega_{15}$	242		A
$\omega_{16}$	266		A
$\omega_{19}$	285	275	A
$\omega_{21}$	335	315	A
$\omega_{22}$	376		A
$\omega_{23}$	380		A
$\omega_{26}$	406		A
$\omega_{28}$	454		A
$\omega_{30}$	492	468	A
$\omega_{34}$	620		A

structure. The discrepancy in the number of the phonon modes with the  $P1$  structure is due to a lot of factors. Primarily, the high-temperature anharmonic effects are dominant and together with the structural phase transition greatly broaden the peak line width. Also, the phonon modes become too weak to be visible, and the strong modes tend to overlap the weak modes.

The low-temperature Raman scattering spectra from 6 to 160 K were consistently fitted with 35 Lorentz peaks,<sup>20</sup> as illustrated in the inset of Figure 4. The mode frequencies at 6 K and atomic motion assignments are summarized in Table 7. The number of phonon modes observed at 6 K is more than that of the expected ones in  $YBaMn_2O_6$  for a monoclinic structure with the  $P2$  space group (see Table 1). This emphasizes the capability of Raman scattering spectroscopy to probe local lattice distortions induced by charge rearrangement and octahedral tilting that cannot be easily identified in the overall average structure.

The vibrational motion assignments of  $YBaMn_2O_6$  were parallel to  $NdBaMn_2O_6$ <sup>13</sup> at 20 K and other perovskite manganites<sup>2,26–30</sup> (see Table 7). The phonon frequencies of

**Table 7. Phonon Frequencies of YBaMn<sub>2</sub>O<sub>6</sub> at 6 K and Phonon Frequencies of NdBaMn<sub>2</sub>O<sub>6</sub> at 20 K with their Main Atomic Motion Assignments<sup>a</sup>**

phonon mode	frequency (cm <sup>-1</sup> )		atomic motions
	YBaMn <sub>2</sub> O <sub>6</sub>	NdBaMn <sub>2</sub> O <sub>6</sub>	
	6 K	20 K	
$\omega_1$	103		mixed vibrations from Y and Ba atoms
$\omega_2$	107		
$\omega_3$	123	117	
$\omega_4$	138		
$\omega_5$	148		
$\omega_6$	161		
$\omega_7$	168	177	
$\omega_8$	179		
$\omega_9$	187		
$\omega_{10}$	195		
$\omega_{11}$	205		
$\omega_{12}$	214		
$\omega_{13}$	227		
$\omega_{14}$	234		
$\omega_{15}$	255		
$\omega_{16}$	267		
$\omega_{17}$	289		
$\omega_{18}$	298		
$\omega_{19}$	307	296	
$\omega_{20}$	312		
$\omega_{21}$	342	332	
$\omega_{22}$	370		
$\omega_{23}$	378		Jahn–Teller distortions
$\omega_{24}$	397		
$\omega_{25}$	408		
$\omega_{26}$	418		
$\omega_{27}$	452		
$\omega_{28}$	477	442	
$\omega_{29}$	491		
$\omega_{30}$	507	489	
$\omega_{31}$	514		
$\omega_{32}$	552		
$\omega_{33}$	572		
$\omega_{34}$	608	600	
$\omega_{35}$	659	653	

<sup>a</sup>The data for NdBaMn<sub>2</sub>O<sub>6</sub> is adapted from ref 13. No subject to Copyright.

YBaMn<sub>2</sub>O<sub>6</sub> were divided into four regions. The first region had frequencies <200 cm<sup>-1</sup> and mainly involved vibrations from Y and Ba atoms (Figures 5 and 6). The second region had modes between 200 and 400 cm<sup>-1</sup> and was due to MnO<sub>6</sub> octahedral distortions from either an out-of-phase rotation or octahedral tilting and bending (Figures 7 and 8). The third region had frequencies between 400 and 600 cm<sup>-1</sup> primarily due to Jahn–Teller stretching (Figures 9 and 10). Finally, the fourth region had frequencies >600 cm<sup>-1</sup> and contained the oxygen cage breathing modes (Figure 10).

The detailed temperature-dependent evolution of the phonon frequency, line width, and normalized intensity of the peaks in each region are illustrated in Figures 5–10. Notably, the intensities were normalized at 200 K. The phonon peaks that can be monitored from 6 to 600 K were fitted with

the anharmonic model. The frequency above the magnetic ordering (>200 K) and below the structural phase transition temperature (<520 K) was used to obtain the best fit line of the anharmonic model, expressed as follows:<sup>31</sup>

$$\omega(T) = \omega_0 + A \left( 1 + \frac{2}{\exp\left(\frac{\Theta}{T}\right) - 1} \right) \quad (1)$$

In this model,  $\omega_0$  is the intrinsic frequency of the optical phonon mode,  $\Theta$  is the Debye temperature, and  $A$  is the anharmonic coefficient. The following values were obtained by fitting parameters for the Jahn–Teller mode at 496 cm<sup>-1</sup> (Figure 10a):  $\omega_0 \approx 522$  cm<sup>-1</sup>,  $A \approx -23$  cm<sup>-1</sup>, and  $\Theta \approx 1000$  K.<sup>7</sup> The negative value of the anharmonic coefficient  $A$  corresponds to the increase in the thermal motion as the temperature increases, which results in a phonon frequency decrease. The thin solid line in Figures 5c,d, 6c, 7c, 8a, and 10b represents the theoretical predictions based on eq 1.

Notable features and discontinuities were observed at the phase transition temperatures of approximately 520, 480, and 200 K deviating from the anharmonic model predictions. At the structural phase transition temperature of approximately 520 K, the phonon intensities of the remaining modes were further reduced by over half at 480 K. The breathing and Jahn–Teller modes became indistinguishable at high temperatures. Large broadening in line width, which began at approximately 480 K, was also noted. The disappearance of these phonon modes indicated the metallic behavior of the material. The phonon modes exhibited a dramatic increase in intensity at approximately 200 K. This particularly applies to those phonon peaks between 360 and 440 cm<sup>-1</sup>, mainly involving MnO<sub>6</sub> octahedra tilting and bending motions. This phenomenon marks the onset of charge and orbital ordering. At temperatures <200 K, the phonon modes  $\omega_3$ ,  $\omega_5$ ,  $\omega_7$ ,  $\omega_8$ ,  $\omega_9$ ,  $\omega_{10}$ ,  $\omega_{12}$ ,  $\omega_{13}$ ,  $\omega_{13}$ ,  $\omega_{16}$ ,  $\omega_{17}$ ,  $\omega_{24}$ ,  $\omega_{25}$ ,  $\omega_{32}$ ,  $\omega_{33}$ , and  $\omega_{34}$  appeared at approximately 103, 123, 148, 179, 187, 195, 205, 227, 234, 289, 298, 397, 408, 552, 572, and 608 cm<sup>-1</sup>, respectively. The activation of these phonon peaks supports the formation of superstructures due to charge and orbital ordering.<sup>12</sup>

In the following section, we detail the anomalies in the phonon frequencies at the phase transition temperatures, starting with the peaks involved with Y and Ba motions, which are displayed in Figures 5 and 6. We observed an approximately 4 cm<sup>-1</sup> splitting of 105 cm<sup>-1</sup> into  $\omega_1 \approx 103$  cm<sup>-1</sup> and  $\omega_2 \approx 107$  cm<sup>-1</sup> at temperatures <200 K shown in Figure 5b. Similarly, the phonon peak centered at 163 cm<sup>-1</sup> at approximately 200 K appeared as two intense peaks at  $\omega_6 \approx 161$  cm<sup>-1</sup> and  $\omega_7 \approx 168$  cm<sup>-1</sup>, as shown in Figure 6c. Moreover, the magnetic phase transition at 200 K was also marked by a dramatic increase in the intensity of phonon peaks,  $\omega_3$ ,  $\omega_5$ ,  $\omega_8$ ,  $\omega_9$ , and  $\omega_{10}$ , positioned at approximately 123, 148, 179, 187, and 195 cm<sup>-1</sup>, respectively (see Figure 6). Figure 5d displays the temperature dependences of the phonon frequency, line width, and normalized intensity of  $\omega_4$  peak at approximately 138 cm<sup>-1</sup>. A discontinuity in intensity was apparent across the phase transition temperatures (200 and 520 K). Discontinuities in the line width were noted at approximately 200, 480, and 520 K, and a large broadening was observed at 480 K. Deviations from the anharmonic behavior were observed for the phonon frequency at 200 and 480 K.

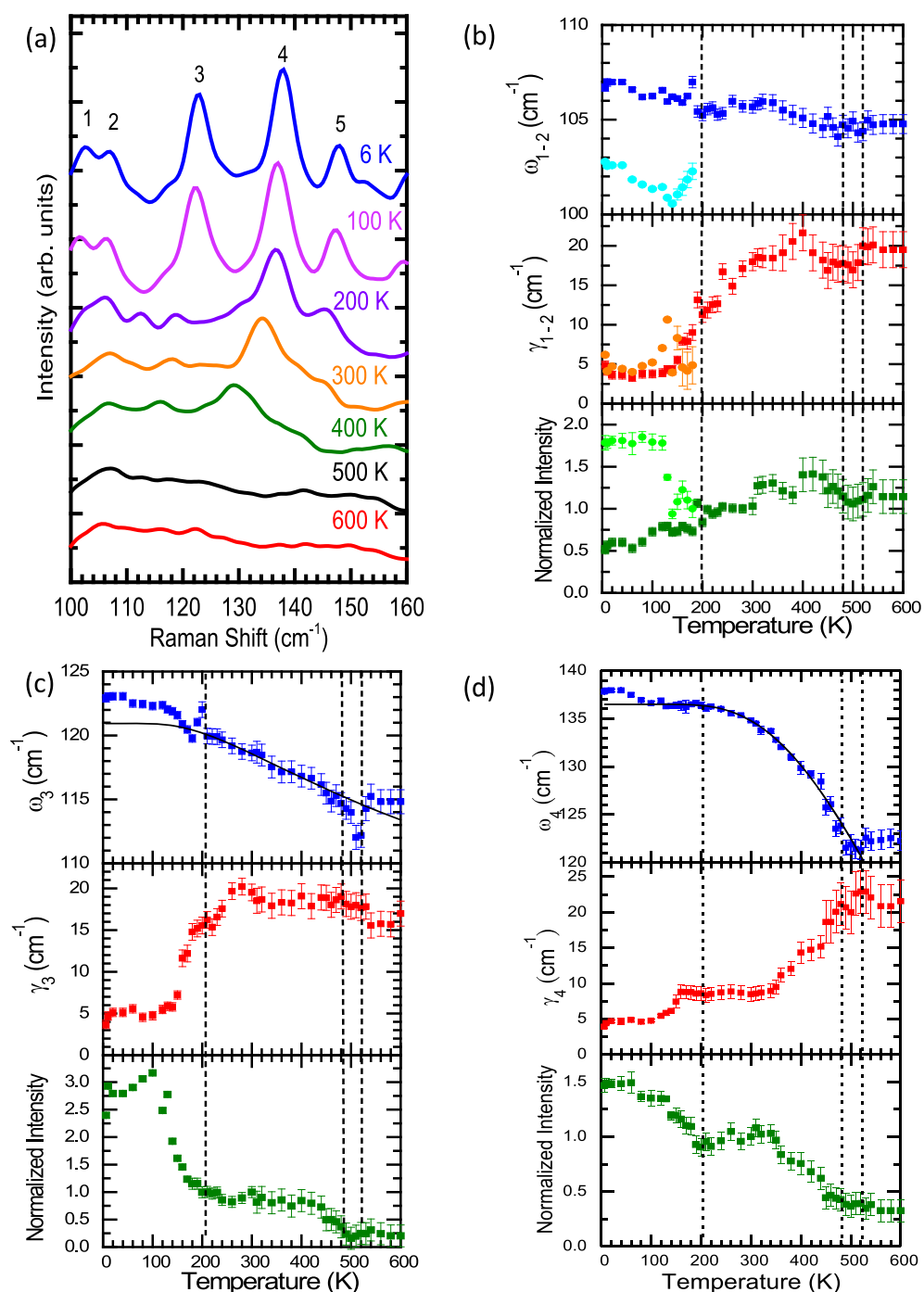


**Figure 5.** (a) Temperature dependence of the unpolarized Raman scattering spectra of  $\text{YBaMn}_2\text{O}_6$  for frequencies between 100 and 160  $\text{cm}^{-1}$ . The temperature dependence of frequency, line width, and normalized intensity of (b)  $\omega_{1-2}$ , (c)  $\omega_3$ , and (d)  $\omega_4$  modes. The vertical dashed lines denote the phase transition temperatures at 200, 480, and 520 K. The thin solid line is the fitting results obtained with the anharmonic model.

Figures 7 and 8 present the temperature dependences of phonon peaks of the  $\text{MnO}_6$  octahedra bending and tilting at frequencies between 210 and 360  $\text{cm}^{-1}$ . We highlight the anomalies in phonon frequency, line width, and normalized intensity of  $\omega_{17-20}$  phonon peaks in Figure 8b. At room temperature, the Raman scattering spectrum was fitted with a main Lorentz peak<sup>20</sup> at approximately 298  $\text{cm}^{-1}$  and a side peak centered near 312  $\text{cm}^{-1}$ . At temperatures <200 K, four phonon peaks were distinctly observed at approximately 289, 298, 307, and 312  $\text{cm}^{-1}$  (see Figure 8a). Similar peak frequency behaviors were noted for phonon modes  $\omega_{11-14}$

(see Figure 7b). The phonon mode  $\omega_{21}$ , as presented in Figure 8c, appears as a double peak centered at approximately 334 and 345  $\text{cm}^{-1}$  at room temperature. It becomes a single peak centered at approximately 342  $\text{cm}^{-1}$  at temperatures <200 K, which contrasts with the split exhibited by  $\omega_{17-20}$ . Moreover, at high temperatures, the  $\omega_{21}$  phonon peak appeared as a single peak near the structural phase transition at 520 K. A reduction of the phonon intensities by more than half across the phase transitions was also observed in addition to the anomalous broadening at high temperatures. These anomalies involving phonon modes associated with  $\text{MnO}_6$  octahedra tilting and

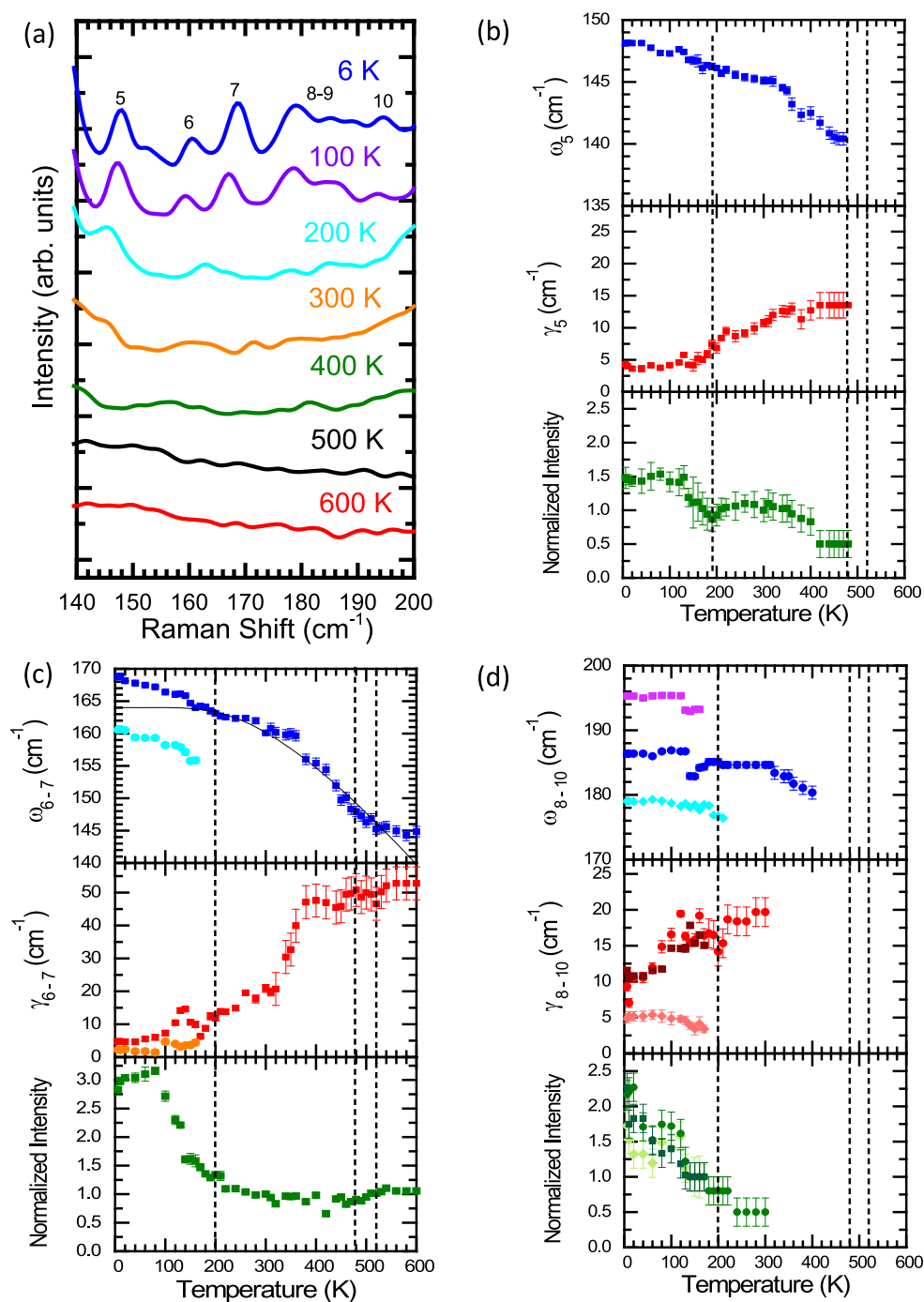


**Figure 6.** (a) Temperature dependence of the unpolarized Raman scattering spectra of  $\text{YBaMn}_2\text{O}_6$  for frequencies between 140 and  $200\text{ cm}^{-1}$ . The temperature dependence of frequency, line width, and normalized intensity of (b)  $\omega_5$ , (c)  $\omega_{6-7}$ , and (d)  $\omega_{8-10}$  modes. The vertical dashed lines denote the phase transition temperatures at 200, 480, and 520 K. The thin solid line is the fitting results obtained with the anharmonic model.

bending modes indicate the sensitivity of these atomic motions during the phase transitions. The atomic motions also indicate the charge rearrangement at 200 K.

Figures 9a and 10a display the temperature-dependent Jahn–Teller modes. Figure 10b describes the frequency, line width, and normalized intensity of the phonon modes positioned at approximately 507 and  $514\text{ cm}^{-1}$ , labeled  $\omega_{30}$  and  $\omega_{31}$ , respectively. The Jahn–Teller modes appeared as clear doublets at temperatures  $<200\text{ K}$  and were accompanied by a more than 4-fold increase in intensity. In contrast with the phonon softening observed in most A-type antiferromagnetic

oxides,<sup>28,32</sup> we observed a pronounced hardening below the magnetic phase transition temperature. Although this contrasts with the observed phonon softening in  $\text{NdBaMn}_2\text{O}_6$ ,<sup>13</sup> it accords with other studies that revealed that CE-type antiferromagnetic structures favor phonon hardening.<sup>33,34</sup> The temperature-dependent breathing modes  $\omega_{34-35}$  are displayed in Figure 10a,c. The breathing mode appears as a broad peak at room temperature, which was resolved into two peaks at approximately 620 and  $642\text{ cm}^{-1}$ . A third breathing mode positioned at approximately  $608\text{ cm}^{-1}$  was also identified at room temperature, which was very weak and fell short of our

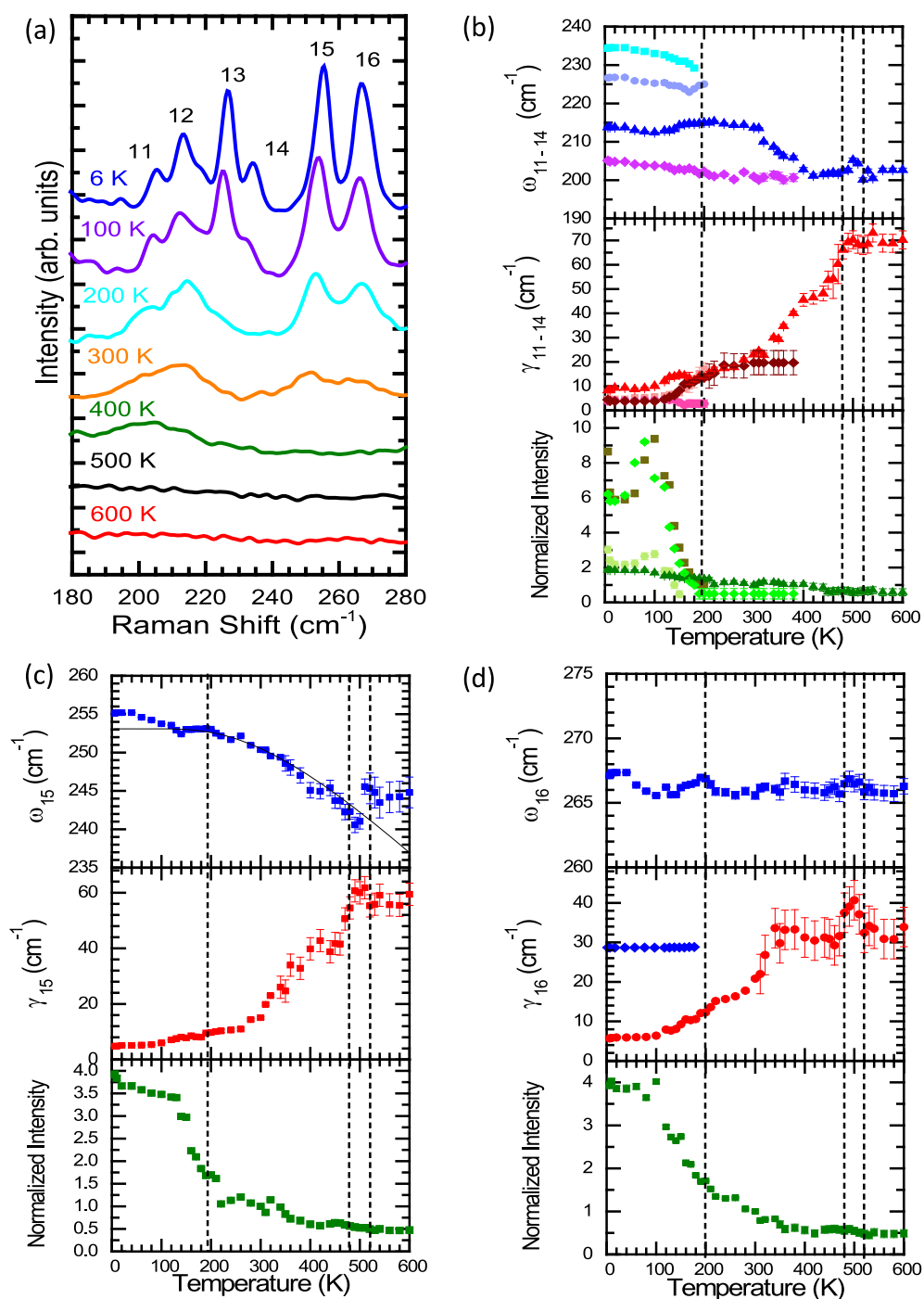


**Figure 7.** (a) Temperature dependence of the unpolarized Raman scattering spectra of YBaMn<sub>2</sub>O<sub>6</sub> for frequencies between 180 and 280 cm<sup>-1</sup>. The temperature dependence of frequency, line width, and normalized intensity of (b)  $\omega_{11-14}$ , (c)  $\omega_{15}$ , and (d)  $\omega_{16}$  modes. The vertical dashed lines denote the phase transition temperatures at 200, 480, and 520 K. The thin solid line is the fitting results obtained with the anharmonic model.

cutoff intensity. The 608 cm<sup>-1</sup> peak gradually increased in intensity at temperatures <200 K, and a triplet peak was observed at 170 down to 140 K. Notably, the 620 cm<sup>-1</sup> breathing mode appeared split into two centered at approximately 608 and 659 cm<sup>-1</sup> at temperatures <140 K, reflecting the charge and orbital orderings. Near the structural phase transition temperature, the breathing modes greatly reduced in intensity and could no longer be distinguished (inset of Figure 10a).

Next, we discuss the large deviation from the anharmonic model at temperatures under the charge/orbital ordering and

magnetic ordering temperatures noted for the Jahn–Teller mode shown in Figure 10b, wherein  $\omega_{30}$  positioned at approximately 496 cm<sup>-1</sup>. This mode mainly contained Mn–O stretching vibrations along the *c*-axis. Deviations from the anharmonic model have been noted for materials with strong lattice, charge, and spin correlations. We ruled out the contributions of thermal lattice expansion because anharmonic effects generally have negligible contributions at low temperatures.<sup>31</sup> A hardening of more than 10 cm<sup>-1</sup> was exhibited by this mode. We attribute this to the renormalization of the phonon frequency that was caused by magnetic ordering and is

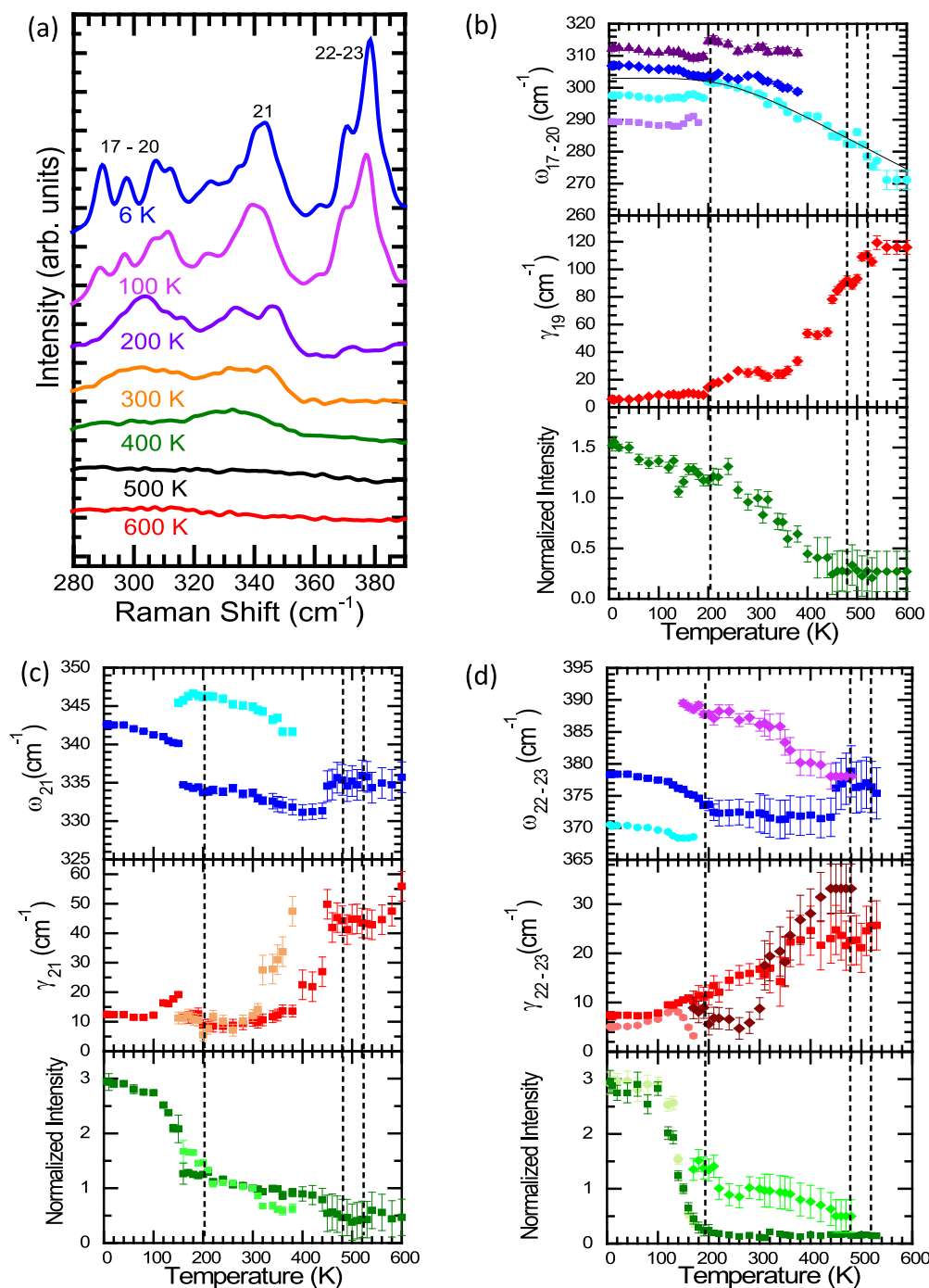


**Figure 8.** (a) Temperature dependence of the unpolarized Raman scattering spectra of  $\text{YBaMn}_2\text{O}_6$  for frequencies between 280 and 390  $\text{cm}^{-1}$ . The temperature dependence of frequency, line width, and normalized intensity of (b)  $\omega_{17-20}$  (c)  $\omega_{21}$ , and (d)  $\omega_{22-23}$  modes. The vertical dashed lines denote the phase transition temperatures at 200, 480, and 520 K. The thin solid line is the fitting results obtained with the anharmonic model.

a signature of spin–phonon coupling. This shift in phonon frequency due to spin–phonon coupling can be described as follows:<sup>28</sup>

$$\Delta\omega(T) \approx \lambda \langle S_i \cdot S_j \rangle \approx 6\lambda \left( \frac{M(T)}{M_s} \right)^2 \quad (2)$$

In this model, the spin–phonon coupling factor,  $\lambda$ , is multiplied by the nearest neighbor spin correlation, given by  $\langle S_i \cdot S_j \rangle$ , to obtain the renormalization of the phonon frequency,  $\Delta\omega(T)$ . Here,  $\langle S_i \cdot S_j \rangle$  was estimated from the square of  $M(T)/$

$M_s$ , where  $M(T)$  is the sublattice magnetization per magnetic ion and  $M_s$  is the saturation magnetization. The factor of six gives the number of nearest neighbors. To illustrate that the observed hardening is a consequence of the magnetic ordering, we plotted the magnetic susceptibility contribution with the phonon renormalization. The described magnetic susceptibility is a sum of the parallel and perpendicular contributions, expressed as  $\chi = \chi_{\parallel} + \chi_{\perp}$ , which is appropriate for an  $ab$  twin structure. Figure 11 displays a linear relationship between the square of the magnetic susceptibility and the phonon renormalization that confirms the spin–phonon coupling in

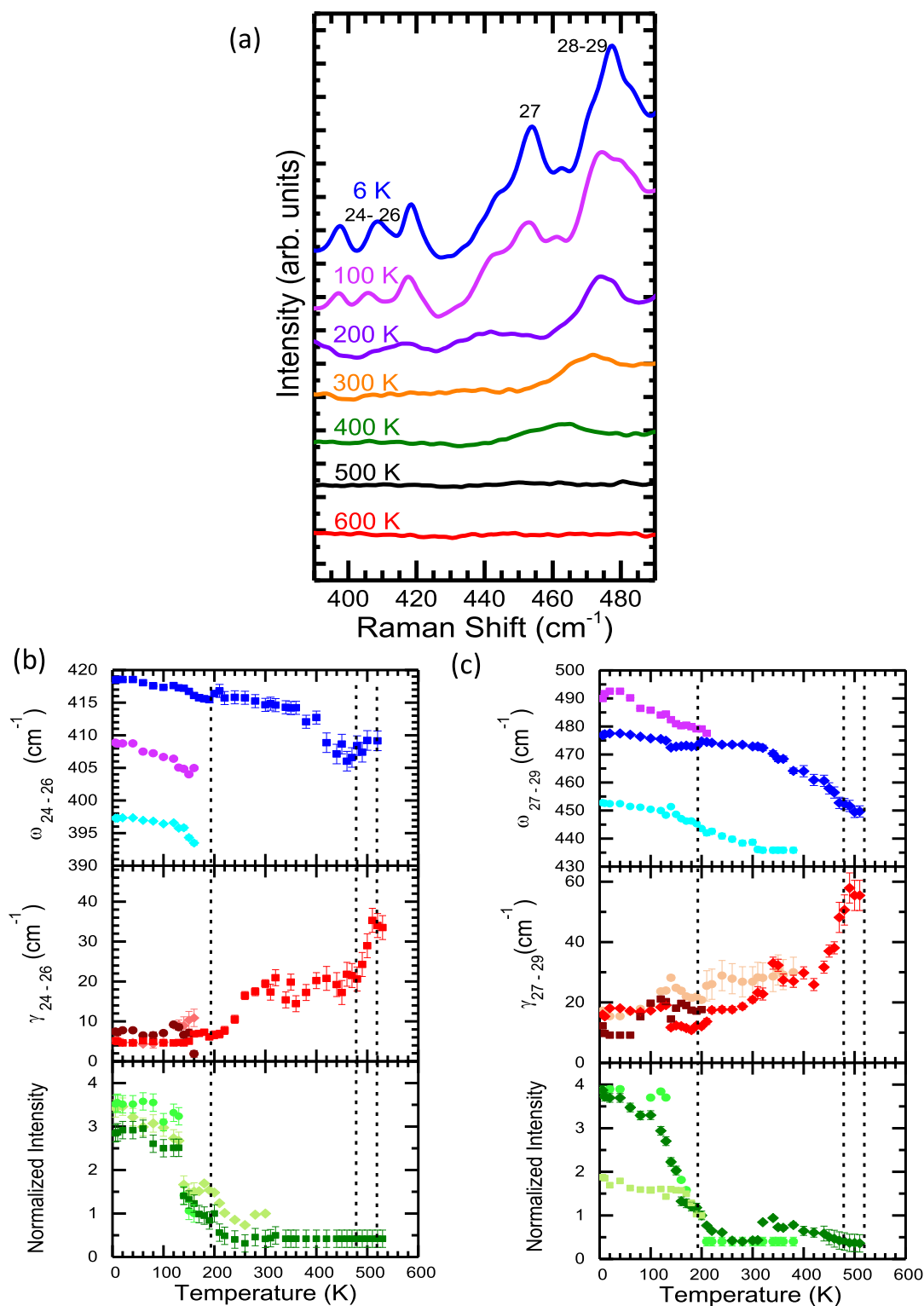


**Figure 9.** (a) Temperature dependence of the unpolarized Raman scattering spectra of  $\text{YBaMn}_2\text{O}_6$  for frequencies between 390 and 490  $\text{cm}^{-1}$ . The temperature dependence of frequency, line width, and normalized intensity of (b)  $\omega_{24-25}$  and (c)  $\omega_{27-29}$  modes. The vertical dashed lines denote the phase transition temperatures at 200, 480, and 520 K. The thin solid line is the fitting results obtained with the anharmonic model.

the present study. Moreover, linear dependence was observed at temperatures  $<T_N = 200$  K, whereas a departure from this linear relationship was observed at low temperatures  $<20$  K. This behavior agrees with those observed in the stretching mode of multiferroics such as  $\text{Cu}_2\text{OCl}_2$ ,<sup>35</sup>  $\text{BiFeO}_3$ ,<sup>36</sup> and  $\text{NiO}$ ,<sup>37</sup> which exhibited spin–phonon coupling.

### 3. CONCLUSIONS

Spectroscopic ellipsometry and Raman scattering spectroscopy were used to determine the correlation between the temperature-dependent optical response and complex phase transitions of  $\text{YBaMn}_2\text{O}_6$  single crystals. The room-temperature optical absorption spectrum of  $\text{YBaMn}_2\text{O}_6$  manifested the d–d

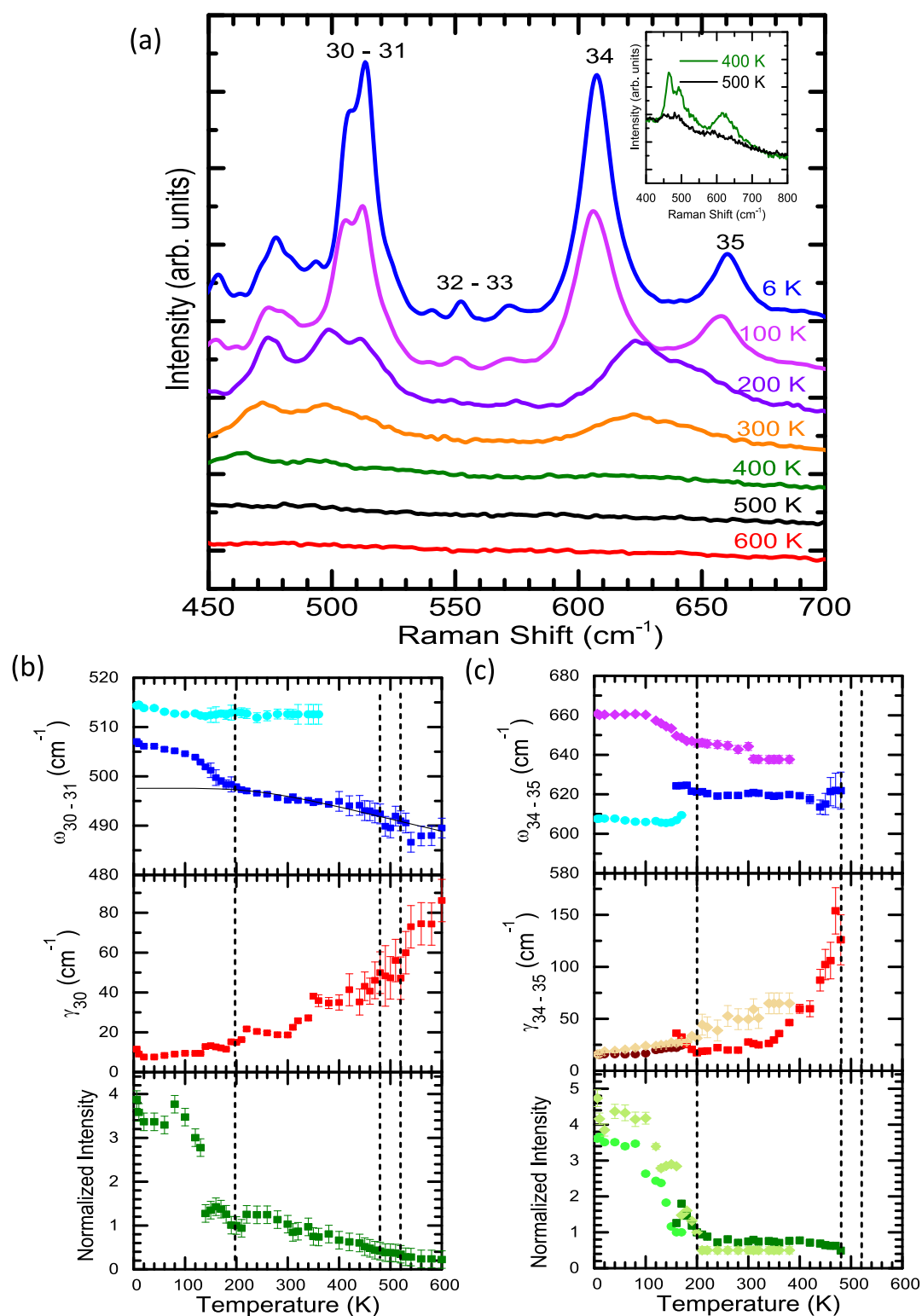


**Figure 10.** (a) Temperature dependence of the unpolarized Raman scattering spectra of  $\text{YBaMn}_2\text{O}_6$  for frequencies between 500 and 700  $\text{cm}^{-1}$ . The inset of (a) illustrates the Jahn–Teller and the breathing modes at 400 and 500 K. The temperature dependence of frequency, line width, and normalized intensity of (b)  $\omega_{30-31}$  and (c)  $\omega_{34-35}$  modes. The vertical dashed lines denote the phase transition temperatures at 200, 480, and 520 K.

on-site transitions in Mn at approximately 1.50 eV. The spectrum also revealed charge-transfer transitions between the 2p states of O and 3d states of Mn at approximately 4.05 and 5.49 eV. The d–d transition peak for  $\text{RBaMn}_2\text{O}_6$  compounds was observed to increase as R radii were decreased. The

enhancement of the intensity of  $\text{MnO}_6$  octahedral bending modes between 360 and 440  $\text{cm}^{-1}$  marked the onset of charge and orbital ordering. This was accompanied by the activation of phonon modes at temperatures <200 K. The Jahn–Teller mode at approximately 496  $\text{cm}^{-1}$  along with the breathing

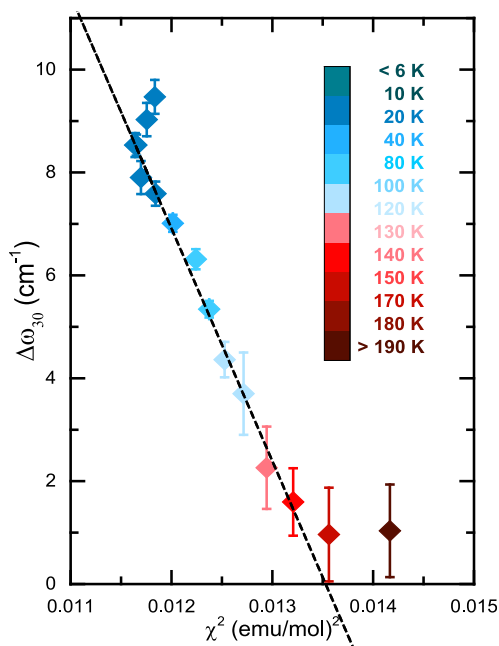


**Figure 11.** Square of the magnetic susceptibility of  $\text{YBaMn}_2\text{O}_6$  plotted against the phonon renormalization of the Jahn–Teller mode at temperatures  $<200$  K.

mode at approximately  $620$  and  $644$   $\text{cm}^{-1}$  exhibited sensitivities to the structural phase transition at  $520$  K, metal–insulator transition at  $480$  K, and the antiferromagnetic ordering transition at  $200$  K. The temperature dependence of the Jahn–Teller mode exhibited an anomalous hardening of approximately  $10$   $\text{cm}^{-1}$  at temperatures  $<200$  K. A linear dependence between the phonon renormalization and the square of the magnetic susceptibility of  $\text{YBaMn}_2\text{O}_6$  was exhibited at temperatures  $<200$  K, thus indicating the establishment of spin–phonon coupling. These phenomena confirm the existence of a strong correlation between the lattice, charge, and spin degrees of freedom in  $\text{YBaMn}_2\text{O}_6$ .

#### 4. EXPERIMENTAL SECTION

$\text{YBaMn}_2\text{O}_6$  single crystals were prepared through a floating zone method. The preparation method is similar to those for  $\text{SmBaMn}_2\text{O}_6$ <sup>38</sup> and  $\text{NdBaMn}_2\text{O}_6$ <sup>39</sup> and entails the use of the precursor powders of  $\text{Y}_2\text{O}_3$ ,  $\text{MnO}_2$ , and  $\text{BaCO}_3$ . The crystals with the (001) surface used in the present study had approximate dimensions of  $2 \times 1.5 \times 0.5$   $\text{mm}^3$ . Magnetic susceptibility measurements of  $\text{YBaMn}_2\text{O}_6$  single crystals shown in Figure 12 revealed an antiferromagnetic phase transition at  $T_N = 200$  K. Spectroscopic ellipsometry measurements were performed at angles of incidence between  $60^\circ$  and  $75^\circ$  using a J. A. Woollam Co. M-2000U ellipsometer over a spectral range of  $0.73$ – $6.42$  eV.<sup>13</sup> The micro-Raman scattering spectra were measured in a backscattering configuration using a laser with an excitation wavelength of  $532$  nm and a SENTERRA spectrometer with a  $1024$  pixel wide charge-coupled detector. The spectral resolution using this spectrometer was typically lower than  $0.5$   $\text{cm}^{-1}$ , and the laser power was kept lower than  $2.0$  mW to avoid thermal damage due to heating effects.<sup>13</sup> The polarized Raman scattering spectra were also obtained in  $Z(\text{YY})\bar{Z}$  and  $Z(\text{XY})\bar{Z}$  scattering configurations. In this Porto notation, the first letter and the last letter represent the propagation directions of the

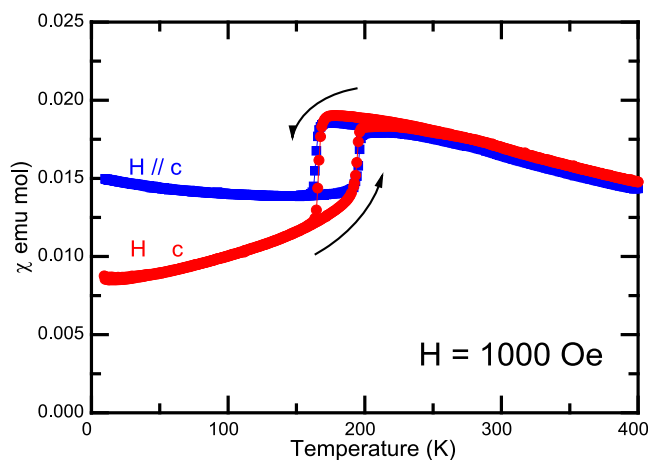


**Figure 12.** Temperature-dependent magnetic susceptibility of the  $\text{YBaMn}_2\text{O}_6$  single crystal.

incident and the scattered light, whereas the letters in parentheses indicate the electric field polarizations of the incident and scattered light, respectively. X, Y, and Z were parallel to the monoclinic [100], [010], and [001] crystal directions, respectively. The temperature-dependent Raman scattering measurements were performed under a continuous-flow helium cryostat for the temperature range of  $6$ – $300$  K, whereas a LINKAM heating stage was used for the temperature range of  $300$ – $600$  K. No substantial differences were observed in the spectra obtained at  $300$  K between the low- and high-temperature setups apart from marginal intensity changes.

#### ■ AUTHOR INFORMATION

##### Corresponding Author

Hsiang-Lin Liu – Department of Physics, National Taiwan Normal University, Taipei 11677, Taiwan; [orcid.org/0000-0003-1960-2776](https://orcid.org/0000-0003-1960-2776); Email: [hliu@ntnu.edu.tw](mailto:hliu@ntnu.edu.tw)

##### Authors

Rea Divina Mero – Department of Physics, National Taiwan Normal University, Taipei 11677, Taiwan

Kirari Ogawa – Department of Material System Science, Yokohama City University, Yokohama 236-0027, Japan

Shigeki Yamada – Department of Material System Science, Yokohama City University, Yokohama 236-0027, Japan

Complete contact information is available at:

<https://pubs.acs.org/10.1021/acsomega.1c02763>

##### Author Contributions

H.L.L. and S.Y. conceived the research idea and were responsible for the experimental design. R.D.M. conducted the experiments. K.O. and S.Y. were responsible for the sample preparation. R.D.M. and H.L.L. drafted the paper. All of the authors have discussed the results and provided comments regarding the manuscript.

##### Notes

The authors declare no competing financial interest.

The data that support the findings of this study are available from the corresponding author upon reasonable request.

## ACKNOWLEDGMENTS

H.L.L. thanks the Ministry of Science and Technology of the Republic of China for its financial support under Grant no. MOST 110-2112-M-003-017. S.Y. thanks the Grant-in-Aid for Scientific Research (no. 24540380) of the Japan Society for the Promotion of Science and Strategic Research Promotion (no. G2503) of Yokohama City University for their financial support.

## REFERENCES

- (1) Akahoshi, D.; Uchida, M.; Tomioka, Y.; Arima, T.; Matsui, Y.; Tokura, Y. Random potential effect near the bicritical region in perovskite manganites as revealed by comparison with the ordered perovskite analogs. *Phys. Rev. Lett.* **2003**, *90*, No. 177203.
- (2) Akahoshi, D.; Okimoto, Y.; Kubota, M.; Kumai, R.; Arima, T.; Tomioka, Y.; Tokura, Y. Charge-orbital ordering near the multicritical point in A-site ordered perovskites  $\text{SmBaMn}_2\text{O}_6$  and  $\text{NdBaMn}_2\text{O}_6$ . *Phys. Rev. B: Condens. Matter Mater. Phys.* **2004**, *70*, No. 064418.
- (3) Ueda, Y.; Nakajima, T. The A-site ordered manganese perovskite and its colossal magnetoresistance. *Prog. Solid State Chem.* **2007**, *35*, 397–406.
- (4) Loktev, V. M.; Pogorelov, Y. G. Peculiar physical properties and the colossal magnetoresistance of manganites (Review). *Low Temp. Phys.* **2000**, *26*, 171–193.
- (5) Kézsmárki, I.; Tomioka, Y.; Miyasaka, S.; Demkó, L.; Okimoto, Y.; Tokura, Y. Optical phase diagram of perovskite colossal magnetoresistance manganites near half doping. *Phys. Rev. B: Condens. Matter Mater. Phys.* **2008**, *77*, No. 075117.
- (6) Moritomo, Y.; Asamitsu, A.; Kuwahara, H.; Tokura, Y. Giant magnetoresistance of manganese oxides with a layered perovskite structure. *Nature* **1996**, *380*, 141–144.
- (7) Nabi, M.; Gupta, D. C. Study of the magneto-electronic, optical, thermal and thermoelectric applications of double perovskites  $\text{Ba}_2\text{MTaO}_6$  ( $M = \text{Er, Tm}$ ). *RSC Adv.* **2019**, *9*, 15852–15867.
- (8) Mir, S. A.; Gupta, D. C. Systematic investigation of the magneto-electronic structure and optical properties of new halide double perovskites  $\text{Cs}_2\text{NaMCl}_6$  ( $M = \text{Mn, Co and Ni}$ ) by spin polarized calculations. *RSC Adv.* **2020**, *10*, 26277–26287.
- (9) Mir, S. A.; Gupta, D. C. Scrutinizing the stability and exploring the dependence of thermoelectric properties on band structure of 3d-3d metal-based double perovskites  $\text{Ba}_2\text{FeNiO}_6$  and  $\text{Ba}_2\text{CoNiO}_6$ . *Sci. Rep.* **2021**, *11*, No. 10506.
- (10) Nakajima, T.; Kageyama, H.; Yoshizawa, H.; Ueda, Y. Structures and electromagnetic properties of new metal-ordered manganites:  $\text{RBaMn}_2\text{O}_6$  ( $R = \text{Y}$  and rare-earth elements). *J. Phys. Soc. Jpn.* **2002**, *71*, 2843–2846.
- (11) Nakajima, T.; Kageyama, H.; Yoshizawa, H.; Ohoyama, K.; Ueda, Y. Ground state properties of the A-site ordered manganites,  $\text{RBaMn}_2\text{O}_6$  ( $R = \text{La, Pr and Nd}$ ). *J. Phys. Soc. Jpn.* **2003**, *72*, 3237–3242.
- (12) Kageyama, H.; Nakajima, T.; Ichihara, M.; Ueda, Y.; Yoshizawa, H.; Ohoyama, K. New stacking variations of the charge and orbital ordering in the metal-ordered manganite  $\text{YBaMn}_2\text{O}_6$ . *J. Phys. Soc. Jpn.* **2003**, *72*, 241–244.
- (13) Mero, R. D.; Ogawa, K.; Yamada, S.; Liu, H.-L. Optical study of the electronic structure and lattice dynamics of  $\text{NdBaMn}_2\text{O}_6$  single crystals. *Sci. Rep.* **2019**, *9*, No. 18164.
- (14) Nakajima, T.; Kageyama, H.; Ueda, Y. Successive phase transitions in a metal-ordered manganite perovskite  $\text{YBaMn}_2\text{O}_6$ . *J. Phys. Chem. Solids* **2002**, *63*, 913–916.
- (15) Nakajima, T.; Kageyama, H.; Ichihara, M.; Ohoyama, K.; Yoshizawa, H.; Ueda, Y. Anomalous octahedral distortion and multiple phase transitions in the metal-ordered manganite  $\text{YBaMn}_2\text{O}_6$ . *J. Solid State Chem.* **2004**, *177*, 987–999.
- (16) Williams, A. J.; Attfield, J. P. Ferro-orbital order in the charge- and cation-ordered manganite  $\text{YBaMn}_2\text{O}_6$ . *Phys. Rev. B - Condens. Matter Mater. Phys.* **2005**, *72*, No. 024436.
- (17) Williams, A. J.; Attfield, J. P.; Redfern, S. A. T. High-temperature orbital, charge, and structural phase transitions in the cation-ordered manganites  $\text{TbBaMn}_2\text{O}_6$  and  $\text{YBaMn}_2\text{O}_6$ . *Phys. Rev. B: Condens. Matter Mater. Phys.* **2005**, *72*, No. 184426.
- (18) Zakharov, D. V.; Deisenhofer, J.; Von Nidda, H.-A. K.; Loidl, A.; Nakajima, T.; Ueda, Y. Electron spin resonance across the charge-ordering transition in  $\text{YBaMn}_2\text{O}_6$ . *Phys. Rev. B* **2008**, *78*, No. 235105.
- (19) Gao, Q.-Q.; Li, J.-B.; Li, G.-N.; Rao, G.-H.; Luo, J.; Liu, G.-Y.; Liang, J.-K. Spin glass behavior in A-site ordered  $\text{YBaMn}_2\text{O}_6$  compound. *J. Appl. Phys.* **2013**, *114*, No. 053901.
- (20) Wooten, F. *Optical Properties of Solids*; Academic Press: New York, 1972.
- (21) Noh, T. W. W.; Jung, J. H. H.; Lee, H. J. J.; Kim, K. H. H.; Yu, J.; Choi, E. J. J.; Moritomo, Y.; Moritomo, Y. Optical properties of perovskite manganites. *J. Korean Phys. Soc.* **2000**, *36*, 392–397.
- (22) Choi, W. S.; Taniguchi, K.; Moon, S. J.; Seo, S. S. A.; Arima, T.; Hoang, H.; Yang, I. S.; Noh, T. W.; Lee, Y. S. Electronic structure and anomalous band-edge absorption feature in multiferroic  $\text{MnWO}_4$ : An optical spectroscopic study. *Phys. Rev. B: Condens. Matter Mater. Phys.* **2010**, *81*, 1–7.
- (23) Kim, M. W.; Moon, S. J.; Jung, J. H.; Yu, J.; Parashar, S.; Murugavel, P.; Lee, J. H.; Noh, T. W. Effect of orbital rotation and mixing on the optical properties of orthorhombic  $\text{RMnO}_3$  ( $R = \text{La, Pr, Nd, Gd, and Tb}$ ). *Phys. Rev. Lett.* **2006**, *96*, No. 247205.
- (24) Lee, H. J.; Jung, J. H.; Lee, Y. S.; Ahn, J. S.; Noh, T. W.; Kim, K. H.; Cheong, S.-W. Optical properties of a  $\text{Nd}_{0.7}\text{Sr}_{0.3}\text{MnO}_3$  single crystal. *Phys. Rev. B* **1999**, *60*, S251–S257.
- (25) Fateley, W. G.; McDevitt, N. T.; Bentley, F. F. Infrared and Raman Selection Rules for Lattice Vibrations: The Correlation Method. *Appl. Spectrosc.* **1971**, *25*, 155–173.
- (26) Abrashev, M. V.; Bäckström, J.; Börjesson, L.; Popov, V. N.; Chakalov, R. A.; Kolev, N.; Meng, R.-L.; Iliev, M. N. Raman spectroscopy of  $\text{CaMnO}_3$  mode assignment and relationship between Raman line intensities and structural distortion. *Phys. Rev. B* **2002**, *65*, No. 184301.
- (27) Iliev, N.; Abrashev, M.; Lee, H.-G.; Popov, V.; Sun, Y.; Thomsen, C.; Meng, R.; Chu, C. Raman active phonons in orthorhombic  $\text{YMnO}_3$  and  $\text{LaMnO}_3$ . *J. Phys. Chem. Solids* **1998**, *59*, 1982–1984.
- (28) Granado, E.; García, A.; Sanjurjo, J. A.; Rettori, C.; Torriani, I.; Prado, F.; Sánchez, R. D.; Caneiro, A.; Oseroff, S. B. Magnetic ordering effects in the Raman spectra of  $\text{La}_{1-x}\text{Mn}_x\text{O}_3$ . *Phys. Rev. B* **1999**, *60*, 11879–11882.
- (29) Silva, R. X.; Castro Júnior, M. C.; Yáñez-Vilar, S.; Andújar, M. S.; Mira, J.; Señaris-Rodríguez, M. A.; Paschoal, C. W. A. Spin-phonon coupling in multiferroic  $\text{Y}_2\text{CoMnO}_6$ . *J. Alloys Compd.* **2017**, *690*, 909–915.
- (30) Silva, R. X.; Reichlova, H.; Marti, X.; Barbosa, D. A. B.; Lufaso, M. W.; Araujo, B. S.; Ayala, A. P.; Paschoal, C. W. A. Spin-phonon coupling in  $\text{Gd}(\text{Co}_{1/2}\text{Mn}_{1/2})\text{O}_3$  perovskite. *J. Appl. Phys.* **2013**, *114*, No. 194120.
- (31) Balkanski, M.; Wallis, R. F.; Haro, E. Anharmonic effects in light scattering due to optical phonons in silicon. *Phys. Rev. B* **1983**, *28*, 1928–1934.
- (32) Mansouri, S.; Jandl, S.; Mukhin, A.; Ivanov, V. Y.; Balbashov, A. A comparative Raman study between  $\text{PrMnO}_3$ ,  $\text{NdMnO}_3$ ,  $\text{TbMnO}_3$ , and  $\text{DyMnO}_3$ . *Sci. Rep.* **2017**, *7*, No. 13796.
- (33) Asselin, S.; Jandl, S.; Fournier, P.; Mukhin, A. A.; Ivanov, V. Y.; Balbashov, A. M. Resonant micro-Raman study of  $\text{Nd}_{0.5}\text{Sr}_{0.5}\text{MnO}_3$ . *J. Phys.: Condens. Matter* **2005**, *17*, 5247–5254.
- (34) Choi, K.-Y.; Lemmens, P.; Guntherodt, G.; Pattabiraman, M.; Rangarajan, G.; Gnezdilov, V. P.; Balakrishnan, G.; McK Paul, D.; Lees, M. R. Raman scattering study of  $\text{Nd}_{1-x}\text{Sr}_x\text{MnO}_3$  ( $x = 0.3, 0.5$ ). *J. Phys.: Condens. Matter* **2003**, *15*, 3333–3342.
- (35) Araújo, B. S.; Arévalo-López, A. M.; Attfield, J. P.; Paschoal, C. W. A.; Ayala, A. P. Spin-phonon coupling in melanothallite  $\text{Cu}_2\text{OCl}_2$ . *Appl. Phys. Lett.* **2018**, *113*, No. 222901.
- (36) Nguyen, T. M. H.; Nguyen, X. N.; Chen, X.-B.; To, X. T.; Lee, S.; Nguyen, T. H.; Yang, I.-S. Study of spin-phonon coupling in

multiferroic BiFeO<sub>3</sub> through Raman spectroscopy. *J. Mol. Struct.* **2020**, *1222*, No. 128884.

(37) Aytan, E.; Debnath, B.; Kargar, F.; Barlas, Y.; Lacerda, M. M.; Li, J. X.; Lake, R. K.; Shi, J.; Balandin, A. A. Spin-phonon coupling in antiferromagnetic nickel oxide. *Appl. Phys. Lett.* **2017**, *111*, No. 252402.

(38) Yamada, S.; Maeda, Y.; Arima, T. Successive electronic transitions and anisotropic properties in a double-perovskite SmBaMn<sub>2</sub>O<sub>6</sub> single crystal. *J. Phys. Soc. Jpn.* **2012**, *81*, No. 113711.

(39) Yamada, S.; Sagayama, H.; Higuchi, K.; Sasaki, T.; Sugimoto, K.; Arima, T. Physical properties and crystal structure analysis of double-perovskite NdBaMn<sub>2</sub>O<sub>6</sub> by using single crystals. *Phys. Rev. B* **2017**, *95*, No. 035101.